AGU PUBLICATIONS

JGR

Journal of Geophysical Research: Space Physics

RESEARCH ARTICLE

10.1002/2013JA019699

Key Points:
- We present a global GNSS scintillation model with significantly high fidelity
- Using SIGMA, we can study intermediate-scale irregularities at high latitudes
- Sensitivity study would help when comparing with observations (follow-up paper)

Correspondence to:
K. B. Deshpande,
kshitija@vt.edu

Citation:
Deshpande, K. B., G. S. Bust, C. R. Clauer, C. L. Rino, and C. S. Carrano (2014), Satellite-beacon Ionospheric-scintillation Global Model of the upper Atmosphere (SIGMA) I: High-latitude sensitivity study of the model parameters, *J. Geophys. Res. Space Physics*, *119*, 4026–4043, doi:10.1002/2013JA019699.

Received 11 DEC 2013
Accepted 22 APR 2014
Accepted article online 29 APR 2014
Published online 27 MAY 2014

Satellite-beacon Ionospheric-scintillation Global Model of the upper Atmosphere (SIGMA) I: High-latitude sensitivity study of the model parameters

K. B. Deshpande[1], G. S. Bust[2], C. R. Clauer[1], C. L. Rino[3], and C. S. Carrano[4]

[1]Electrical and Computer Engineering Department, Virginia Tech, Blacksburg, Virginia, USA, [2]Johns Hopkins University Applied Physics Laboratory, Laurel, Maryland, USA, [3]Rino Consulting, Menlo Park, California, USA, [4]Boston College, Chestnut Hill, Massachusetts, USA

Abstract Complex magnetosphere-ionosphere coupling mechanisms result in high-latitude irregularities that are difficult to characterize using only Global Navigation Satellite System (GNSS) scintillation measurements. However, GNSS observations combined with physical parameters derived from modeling can be used to study the physics of these irregularities. We have developed a full three-dimensional electromagnetic wave propagation model called "Satellite-beacon Ionospheric-scintillation Global Model of the upper Atmosphere" (SIGMA), to simulate GNSS scintillations. This model eliminates the most significant approximation made by the previous simulation approaches about the correlation length of the irregularity. Thus, for the first time, using SIGMA, we can accomplish scintillation simulations of significantly high fidelity. While the model is global, it is particularly applicable at high latitudes as it accounts for the complicated geometry of the magnetic field lines in these regions. Using SIGMA, we simulate the spatial and temporal variations in the GNSS signal phase and amplitude on the ground. In this paper, we present the model and results from a study to determine the sensitivity of the SIGMA outputs to different input parameters. We have deduced from our sensitivity study that the peak to peak (P2P) power gets most affected by the spectral index and line of sight direction, while the P2P phase and standard deviation of the phase (σ_ϕ) are more sensitive to the anisotropy of the irregularity. The sensitivity study of SIGMA narrows the parametric space to investigate when comparing the modeled results to the observations.

1. Introduction and Motivation

Ionospheric scintillations are rapid variations in the amplitude and phase of the radio signals resulting from the electron density irregularities in the ionosphere. Such rapid variations in the radio signals can have deleterious effects on the societal systems. For example, ionospheric irregularities can affect Global Navigation Satellite System (GNSS) and produce scintillations that may cause distortion in the signal's phase and amplitude. As summarized by *Aarons* [1982], the scintillations are frequently observed in the high latitude and equatorial regions.

The study of ionospheric scintillations involves the problem of electromagnetic (EM) wave propagation in random media. An extensive discussion of scintillation theories such as the phase screen theory, Rytov solution, parabolic equation method, and Fresnel-Kirchhoff diffraction formulation can be found in the work of *Yeh and Liu* [1982]. *Costa and Basu* [2002] describe slant propagation of a plane wave through a bidimensional irregularity layer using the Huygens-Fresnel convolution integral. *Fremouw and Secan* [1984], *Secan et al.* [1995], and *Secan et al.* [1997] present Wideband ionospheric scintillation model and its high-latitude upgrade SCINTMOD. These employ a phase screen model introduced by *Rino* [1979] in which the irregularity or a phase screen is characterized by a power law electron density spectrum. *Knepp* [1983] and *Knepp and Nickisch* [2009] discuss the multiple phase screen (MPS) simulation that solves for transionospheric propagation involving a number of layers of ionization and directly computes a realization of the signal received on ground. Each of these layers is characterized by a spatially varying electron density power spectrum. *Béniguel* [2002] introduced a Global Ionospheric Scintillation propagation Model based on the MPS technique. *Béniguel and Hamel* [2011] implemented this model for equatorial regions showing a good agreement of the model with measurements. *Humphreys et al.* [2010] present an equatorial scintillations model for improving the scintillation performance of phase-tracking loops. *Grimault* [1998] demonstrates

a numerical technique also based on MPS, modified to be applicable for cases when the EM wave source is close to the turbulent medium and the receiver is far away. A propagation model by *Gherm et al.* [2000] and *Gherm et al.* [2005a] for scintillations on transionospheric links makes use of the extended Rytov approximation. Based on their work, *Maurits et al.* [2008] modeled the scintillation effects on high-latitude transionospheric paths.

Modeling the random EM wave propagation through ionospheric irregularities at high latitudes has a different set of complications and issues from modeling in the equatorial regions. At high latitudes, the magnetic field is nearly vertical, and the irregularities that extend along the magnetic field over large distances have to be treated carefully. In particular, an approximation often made for the equatorial or statistically based models is that the thickness of the irregularity layer being integrated through is much larger than the scale of the irregularities. While this is true at the equatorial latitudes, where the magnetic field is horizontal and the integration is through the vertically extended regions, it is not true at the high-latitude regions. Another issue at high latitudes, particularly for modeling Global Positioning System (GPS) signals, is that the maximum elevation angle to the GPS satellites gets smaller as you go to higher latitudes ($\sim 46°$ at the geographic pole). This poses a numerical issue since for thick layers and smaller elevation angles, the signal can cut through several hundreds of kilometers horizontally. A third issue is the arbitrary geometry, when considering three coordinate systems: the satellite-receiver line of sight (LOS) system, the irregularity layer (the geographic or geomagnetic) coordinate system, and the magnetic field coordinate system. For such complex geometries, no simplifying approximations can be made, and the high-latitude scintillation problem must be treated as a full three-dimensional (3-D) EM wave propagation problem. To address these issues, we have developed a new 3-D EM random media propagation model: "Satellite-beacon Ionospheric-scintillation Global Model of the upper Atmosphere" (SIGMA). While SIGMA has been developed to be applicable over the entire globe, and for all transionospheric frequencies (low VHF and above), it has been specifically developed to handle the particular complications of the high-latitude scintillation problem. Inside SIGMA we propagate a signal from a moving satellite to the ground through multiple phase screens as illustrated in Figure 1. We first obtain a spatial electron number density distribution from a spectral model for high-latitude irregularities and then utilize a hybrid method that combines the MPS technique with a split-step solution to the forward propagation equation (FPE) [*Rino*, 2010; *Rino and Carrano*, 2011]. As mentioned by *Rino and Carrano* [2011], FPE is the most general way to solve a scintillation problem as it encompasses refraction, diffraction, and the effects of small-scale structure. The split-step method has been used recently by *Ghafoori* [2012] to achieve a physics-based scintillation simulations but at equatorial latitudes.

Radio propagation measurements are sensitive to the small- and intermediate-scale structures, structure transport, and total electron content (TEC). Although TEC measurements are more abundantly available than scintillation measurements, they cannot resolve the small- and intermediate-scale structures. GNSS scintillation measurements alone are insufficient to extract information about these structures. SIGMA can give us a capability to infer the physics of these structure from the scintillation measurements.

Our ultimate goal is to try to have better understanding of the physics of the small- and intermediate-scale ionospheric structures at the high-latitude regions. This can be achieved using the GNSS scintillation observations and observations from other ancillary instruments coupled with the physical and propagation parameters derived from SIGMA. The sensitivity study of SIGMA presented in this paper will be useful when comparing our results with the GNSS observations which will be our follow-up work. The parameters derived from such a comparison and an inverse method can be used to extract the physics of the irregularity involved in the generation of those scintillations. Good examples of the inverse modeling technique can be found in the works of *Keskinen* [2006] and *Carrano et al.* [2012b], where they use the technique to infer turbulence parameters from intensity scintillation data from the low-latitude regions.

In this paper, we investigate the physical, propagation, and geometrical input parameters using a sensitivity analysis of the model. Physical parameters include the inner and outer scales of the irregularity, the power index, and anisotropy of the irregularity spectrum, while propagation parameters consist of altitude, thickness of the irregularity, and the number of layers. Geometrical parameters include the elevation and azimuth of the LOS signal. The outputs from SIGMA are the peak to peak (P2P) variations in the power and phase received on the ground, the GPS scintillation indices S4 (normalized variance of amplitude fluctuations), and σ_ϕ. These outputs are obtained by applying a high-pass filter with a cutoff frequency of 0.1 Hz to the

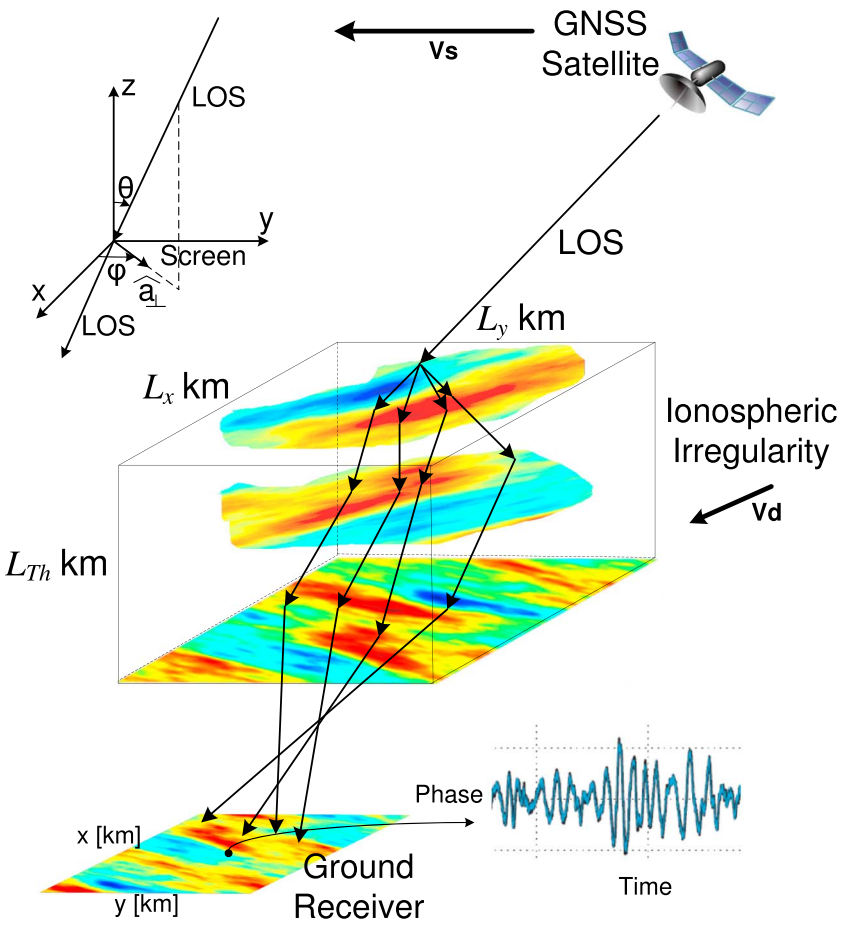

Figure 1. An illustration showing the components covered by SIGMA. The figure is not to scale. Although only three phase screens are shown in the illustration, the number of screens can be changed in the model. The inset coordinates represent the slant geometry of SIGMA.

amplitude and phase on the ground. These are also the observables that can be derived from the high-rate (typically 50 Hz) data collected by the GPS scintillation monitors. The goal of this work is to determine which observables on the ground are the most sensitive to the SIGMA input parameters.

We describe SIGMA and its implementation in section 2. In section 3, we present our results from the sensitivity study of our model with a discussion about the results in section 4. Finally, we summarize our work and describe our future plans in section 5.

2. Description of SIGMA

With a goal to study the physics of the ionospheric irregularities, this work attempts to simulate the 3-D propagation of an obliquely incident satellite signal through an irregularity. The irregularity is assumed to be a set of diffractive phase screens or layers aligned along the magnetic field lines. As defined by *Yeh and Liu* [1982], the phrase "phase screen" is used to depict an assumption that every layer is thin enough to introduce random phase fluctuations in the incident signal that are proportional to the electron content in that layer. On the other hand, the amplitude remains unchanged. As the wave propagates in free space between two layers, fluctuations in the amplitude may start to develop. Similar to an approach described by *Grimault* [1998], in SIGMA, we utilize a hybrid numerical technique with the MPS and a split-step method to propagate a satellite signal through an ionospheric irregularity.

The 3-D random realization of the electron density in the irregularity can be produced by different types of models. For example, first principle numerical simulations of irregularity density fields can be used [*Gondarenko and Guzdar*, 2001, 2003, 2006; *Keskinen et al.*, 2003, 2006] to generate the realization of the

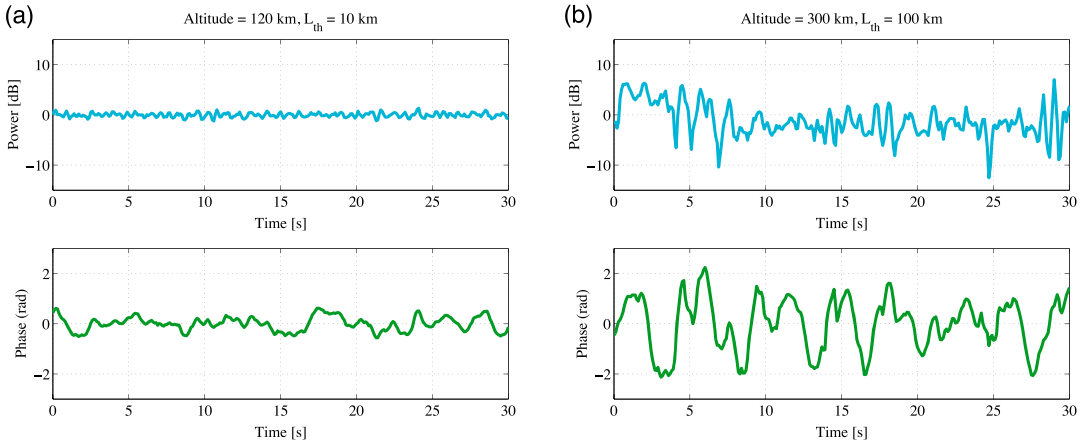

Figure 2. Examples of the power and phase time series on ground modeled using SIGMA at altitudes of (a) 120 km and (b) 300 km with irregularity thickness of 10 km and 100 km, respectively. To generate these time series, we used the remaining input values the same as those introduced later in Table 1.

electron density fields. Another way of generating a random realization of the electron density field could be the use of the empirical spectral models of the density irregularities.

While SIGMA can take in any electron density field, for this study, we use spectral models to generate the density field. In this section, we initially present the ionospheric irregularity spectral model and a coordinate system transformation to obtain the spectral model in a reference coordinate system. Following that, we demonstrate the use of the spectral model to obtain a phase at the bottom of a layer. We then discuss updating the incoming electric field at the bottom of the layer and then obliquely propagating it to the next layer or to the ground. Finally, we briefly describe the split-step method and the simulation procedure of SIGMA. We save either two-dimensional (2-D) snapshots of the spatial complex signal at one-time instance or a time series of the complex signal at the receiver location on the ground. Two examples of the modeled power and phase time series on the ground with different altitudes and irregularity thicknesses are shown in Figure 2. Here the phase and power are subjected to high-pass filtering with 0.1 Hz cutoff frequency, similar to that used for the real observations to eliminate any low-frequency effects including the satellite motion. For the sensitivity study presented in this paper, we use 2-D snapshots at one-time instance, the examples of which will be shown in the later sections of the paper. Since each of the time series simulations demands higher computation time and memory, we base our sensitivity study on the statistics extracted mainly from the 2-D plots.

2.1. Spectral Model

For the ease of implementation and because of insufficient high-latitude empirical and observational electron density data, we begin with the high-latitude power spectral density (PSD) of the electron density fluctuations in an ionospheric irregularity, instead of the actual spatial distribution of electrons in a slab. There are a number of different types of power spectra that can be used, a simple isotropic power law spectrum, a simple anisotropic power law spectrum [*Rufenach*, 1975], and a generalized "Shkarofsky" spectrum [*Shkarofsky*, 1968], to name a few. In our work, we are using a "Hybrid" spectrum introduced by *Costa and Kelley* [1977] for the high-latitude irregularities.

The Hybrid spectrum depicts a Gaussian distribution along the magnetic field in the direction of k'_z and a power law variation in the direction perpendicular to it. The Hybrid spectrum in the irregularity field-aligned irregularity coordinate system (introduced in the next paragraph) is defined as

$$P'_{NH}(\vec{k}') = \frac{a(\gamma_H - 2)}{2\pi^{3/2} k_0^2}\, \Delta N^2 \left(1 + \frac{k_x'^2 + k_y'^2}{k_0^2}\right)^{-\gamma_H/2} \exp\left(-(ak_0)^2 \frac{k_z'^2}{k_0^2}\right), \quad (1)$$

where γ_H is the spectral index, ak_0 depicts the axial ratio (AXR), and k_0 is the wave number associated with the outer scale l_0. The outer scale is the largest spatial dimension of the ionospheric irregularities. $\Delta N = \langle N^2(\vec{r})\rangle^{1/2}$ is the root-mean-square (RMS) of the electron density fluctuations $N(\vec{r})$ which are assumed to be generated by a zero-mean stationary random process. Following works of *Costa and Kelley* [1977]

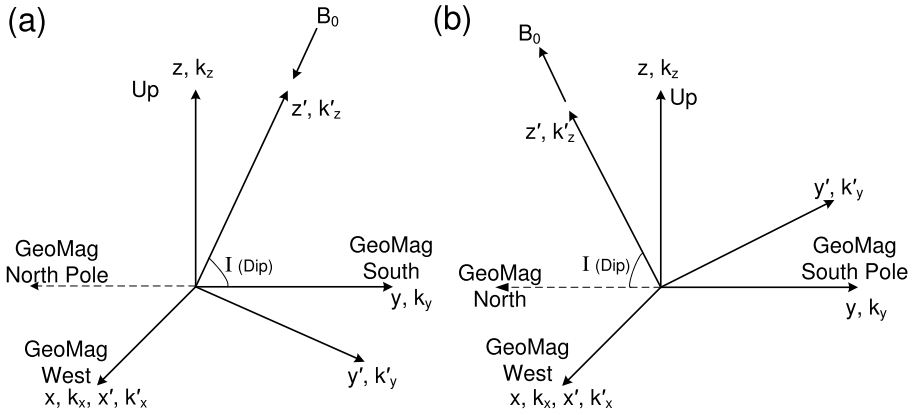

Figure 3. Coordinate transformation from magnetic field-aligned irregularity coordinates to local reference coordinates, (a) Northern and (b) Southern Hemispheres.

and *Gola et al.* [1992], for this study, we assume that the irregularities are field aligned and rod shaped. The Hybrid spectral model considers different variations in the directions parallel and perpendicular to the magnetic field. The axial ratio is a parameter in this spectral model that defines the anisotropy of the rod-shaped irregularities.

The irregularity spectrum is given in terms of the irregularity coordinate system (in primed coordinates), which is assumed to be aligned with the magnetic field B_0. The field-aligned irregularity coordinate system and a reference (topocentric) coordinate system (in unprimed coordinates) centered locally at the receiver location in the Northern Hemisphere are shown in Figure 3a. This figure is adapted from the works of *Rufenach* [1975] and *Costa and Kelley* [1977] and is modified to obtain the transformation in the Southern Hemisphere as shown in Figure 3b. In Figures 3a and 3b, the vertical direction and B_0 define a plane which is aligned with a magnetic meridional plane. Variables $k'_x, k'_{y'}$ and k'_z are the wave number variables in x', y', and z' directions, respectively. Similarly, k_x, k_y, k_z are the wave number variables in x, y, z directions, respectively. z' and k'_z are along B_0, while y' and k'_y are in the meridional plane and are in the direction perpendicular to B_0. x' and k'_x along with x and k_x are in the geomagnetic west direction. z and k_z are vertically up at the receiver location, while y and k_y are in the geomagnetic south direction in a horizontal plane perpendicular to z and k_z. The angle I is the magnetic inclination or dip angle.

2.2. Wave Field at the Bottom of a Phase Screen

As described earlier, the density fluctuations inside an irregularity layer affect the phase of the incoming signal, whereas its amplitude is assumed to be unperturbed. In the absence of diffraction, the phase perturbation at the bottom of an irregularity layer in a continuously displaced coordinate system (CDCS) [*Rino*, 2010] can be given as

$$\Phi(\vec{\rho}) = -\lambda r_e \sec\theta \int_{z_s}^{z_e} N_e(\vec{\rho}_d, z)dz, \tag{2}$$

where $\vec{\rho}$ is the 2-D position vector in the horizontal direction and is given by $\vec{\rho} = x\hat{x} + y\hat{y}$, r_e is the electron radius, and θ is the angle subtended by the LOS vector with the vertical (z-direction) as shown in Figure 1. The LOS vector here is defined from the receiver to the GNSS satellite position. $N_e(\vec{\rho}_d, z)$ is a horizontally displaced random realization of the electron number density of the cold plasma and can be derived from the PSD of the irregularity spectra as

$$N_e(x, y, z) = \Re\left(\mathcal{F}^{-1}\left[\sqrt{P_{NH}}\exp(i2\pi\theta_k)\right]\right), \tag{3}$$

where $\mathcal{F}^{-1}$ stands for the inverse Fourier transform (3-D in this case), θ_k is a statistically independent 3-D random number between 0 to 1, and $\Re$ depicts the real part of the complex numbers. Taking the real part simply ensures that the random realizations of the electron density are real valued. The PSD P_{NH} is P'_{NH} from equation (1) converted to the local coordinate system.

In equation (2), variable z is in the local coordinate system and has integration limits z_s and z_e. The vector $\vec{\rho}_d$ is in the displaced local coordinate system. The CDCS geometry was introduced by *Rino* [2010] to resolve a

problem of significantly increasing support space required to capture the evolution of an obliquely incident field as it propagates through the irregularity. With this, $\vec{\rho}_d = \vec{\rho} + \tan\theta\,\widehat{\mathbf{a}_\perp} z$, where $\widehat{\mathbf{a}_\perp} = [\cos\phi_l, \sin\phi_l]$ is the unit vector of the projection of the LOS vector on the *x*-*y* plane as shown in Figure 1. The zenith angle is θ (complimentary to the elevation angle), and ϕ_l is the azimuth angle of the LOS vector. With these changes, the spatial phase from equation (2) becomes

$$\Phi(\vec{\rho}) = -\lambda r_e \sec\theta \int_{z_s}^{z_e} N_e(\vec{\rho} + \tan\theta\,\widehat{\mathbf{a}_\perp} z, z)dz. \tag{4}$$

For large values of $\tan\theta$ and z, $\vec{\rho}_d$ can get significantly large. In order to have $\vec{\rho}_d$ within the limits, we would have had to make $N_e(\vec{\rho}_d, z)$ large accordingly. But, this would have stretched the computational capacity of SIGMA diminishing its efficiency in generating longer time series. We surpass this computational limitation by imposing periodicity condition on $N_e(\vec{\rho}_d, z)$. This gives us an added advantage of eliminating the edge discontinuity problems, if any.

The wave field propagated through the phase screen will have its phase altered by $\Phi(\vec{\rho})$ and will thus be a different realization of the received electric field. Let $\vec{E}_a(\vec{\rho})$ be an electric field from the satellite or that propagated from the layer *a*. If $\vec{E}_a(\vec{\rho})$ is incident on the next layer *b*, then with $\Phi(\vec{\rho})$ as the perturbed phase at the bottom of layer *b*, the field at the bottom of the layer *b* is given by

$$\vec{E}_b(\vec{\rho}) = \vec{E}_a(\vec{\rho}) \exp(-i\Phi(\vec{\rho})). \tag{5}$$

2.3. Propagation at an Oblique Angle

A satellite signal exhibits variable angle of incidence based on the motion of the satellite. For this, we need to consider a slant propagation. The expression for propagation at an oblique angle can be obtained by generalizing the propagation expression for vertical incidence given by *Rino and Carrano* [2011]. The vertical propagation expression is given by

$$f(\vec{\rho}, z) = \int \widetilde{E}(\vec{\kappa}) \exp(ikg(\vec{\kappa})(z - z_0)) \exp(i\vec{\kappa} \cdot \vec{\rho})\, d\vec{\kappa}, \tag{6}$$

where z is the reference direction along the vertical axis, $z = 0$ is at the top of the irregularity, $z = z_0$ is at the bottom of a layer, and $z - z_0$ can be equal to either the distance between two layers or H_{iono}, the height of the ionospheric irregularity. The 2-D horizontal position vector in the Fourier domain is $\vec{\kappa}$ and is given by $\vec{\kappa} = k_x\hat{k}_x + k_y\hat{k}_y$. The factor $g(\vec{\kappa})$ is defined as $\sqrt{1 - (k_x^2 + k_y^2)/k^2}$, where $k(= 2\pi/\lambda)$ is the wave number or the magnitude of a wave vector and λ is the signal wavelength. Finally, $\widetilde{E}(\vec{\kappa})$ is the electric field in spectral domain at the bottom of a layer and can be obtained by taking a 2-D Fourier transform (FT) of equation (5) as

$$\widetilde{E}(\vec{\kappa}) = \mathcal{F}\,[\vec{E}(\vec{\rho})], \tag{7}$$

where $\mathcal{F}$ is the 2-D forward FT and $\vec{E}(\vec{\rho}) = \vec{E}_b(\vec{\rho})$ from equation (5) at the bottom of the layer *b*.

In the CDCS, we can obtain the propagation at an oblique angle from the following expression:

$$f(\vec{\rho}, z) = \int \widetilde{E}(\vec{\kappa}) \exp(ikg(\vec{\kappa} + \vec{k_\perp})(z - z_0)) \quad \exp(i\tan\theta\,\widehat{\mathbf{a}_\perp} \cdot \vec{\kappa}(z - z_0)) \exp(i\vec{\kappa} \cdot \vec{\rho})\, d\vec{\kappa}, \tag{8}$$

where a spatial variable change of $\vec{\rho}$ and a replacement of $kg(\vec{\kappa})$ was invoked in equation (6) as suggested by *Rino and Carrano* [2011]. The horizontal vector is changed as

$$\rho \longrightarrow \rho + \tan\theta\,\widehat{\mathbf{a}_\perp}(z - z0). \tag{9}$$

$kg(\vec{\kappa})$ is replaced to

$$kg(\vec{\kappa}) \longrightarrow kg(\vec{\kappa} + \vec{k_\perp}) - \tan\theta\,\widehat{\mathbf{a}_\perp} \cdot \vec{\kappa}, \tag{10}$$

where $\vec{k_\perp}$ is the transverse component of $\vec{k_k}$. The wave vector is defined as $\vec{k_k} = k_{kx}\hat{k}_x + k_{ky}\hat{k}_y + k_{kz}\hat{k}_z$, or $\vec{k_k} = k[\sin\theta\cos\phi_l, \sin\theta\sin\phi_l, \cos\theta]$, where k is the magnitude of the wave vector. Here $\vec{k_k}$ can also be written as $[\vec{k_\perp}, k_{kz} = k\,g(\vec{k_\perp})]$.

Table 1. SIGMA Input Parameters[a]

Irregularity	*Parameters*
l_0	Outer scale (2 km)
SpInd	**Spectral index** (3)
ΔN	**RMS electron density** fluctuation (2e11 el/m^3)
AXR	**Axial ratio** (5)
Geographical	*Parameters*
I	Dip angle (73°)
LOS(Elv,Az)	LOS vector **elevation and azimuth** (50°, 160°)
Propagation	*Parameters*
H_{iono}	Altitude (120 km)
N_l	Number of layers (1)
L_{Th}	**Thickness** (10 km)
v_d	Drift velocity (500 m/s)

[a]The parameters we focus our sensitivity study on are shown in boldface.

If the spatial structure in the irregularity is moving with a velocity $\vec{v}_k$, the 3-D irregularity field will move across the LOS field of view. If the field is "frozen-in" and not otherwise evolving in time, we can simulate that motion by simply translating the coordinates of the 3-D irregularity distributions as

$$\vec{\rho} \longrightarrow \vec{\rho} + \vec{v}_k t, \tag{11}$$

where $\vec{v}_k$ is made up of a horizontal "drift" component $\vec{v}_d$, as well as a vertical component v_z. Finally, in addition to the irregularities drifting vertically through a fixed layer, we have to consider the entire layer rising or falling vertically. Typically, we ignore any vertical motions in the simulation, though they can be included as needed. By allowing the 3-D density irregularity field to drift past the LOS as time evolves and allowing the LOS to move as the satellite (or receiver) moves, we are capable of simulating the full 3-D temporal evolution of both motions of the satellite-receiver LOS and drifting of the irregularities. Note that there is nothing in the physics to stop us from simulating more random velocity fields as well as temporal evolution of the irregularity field.

3. Sensitivity Study

The objective of the sensitivity study of SIGMA is to determine which of the observables are the most sensitive to the input parameters. For the Hybrid spectral model we have selected for this sensitivity study, SIGMA depends on eight different physical and propagation parameters. Physical parameters characterize the ionospheric irregularity. They include the outer scale l_0, RMS electron number density ΔN, spectral index *SpInd*, and anisotropy of the irregularity spectrum defined by the axial ratio. The propagation parameters consist of altitude H_{iono}, thickness of the irregularity L_{Th}, number of layers N_l, and drift velocity v_d. Finally, SIGMA also expects some geographical parameters as input. These include the receiver, satellite locations in Earth-centered Earth-fixed (ECEF) coordinates or simply the azimuth and elevation angles of the LOS vector, and the dip angle at the receiver location. Currently, SIGMA assumes a constant dip angle, i.e., a curvature in the field lines is ignored. The receiver and satellite locations are converted into the local coordinate system. All these input parameters are summarized in Table 1. The inputs we focus our sensitivity study on are highlighted in the same table.

In this study, we choose the spatial resolutions in the *x* and *y* directions to be isotropic and equal to 50 m. This is below the anticipated Fresnel scale in the *E* region (~110 m at GPS L1 frequency). We compute the resolution *dz* in the *z* direction such that it satisfies two conditions: first, it is much smaller than the coherence length in the *z* direction and second, the horizontal projection of *dz* is smaller than the Fresnel scale. The value of *dz* comes around 40 m. The horizontal extent in the x and y direction is 20 km (L_x and L_y in Figure 1). But, this may increase when we change L_{Th}.

Each of the input parameters are adjusted independently of the others to isolate the effects of those adjustments on the model's outputs. The "base" values of input parameters are listed in the brackets in Table 1. Currently, we are focusing on five input parameters: the elevation and azimuth angles of the LOS vector, axial ratio, spectral index, thickness of the irregularity, and RMS electron density fluctuations. The base values of these selected parameters are highlighted in Table 1. For this study, we assume weak scattering so that we do not need multiple layers. Thus, we have chosen the base values that result in weak scattering. Also, we chose the base irregularity spectrum parameters such that our assumption of field-aligned and rod-shaped irregularities holds. Furthermore, as we will show later, the base value of the LOS vector direction is not in any preferred direction. Additionally, it was obtained from a real satellite position in the skies above the geographic South Pole, which is the receiver location for most of the sensitivity study runs.

The main reason we chose these parameters is that they represent conditions similar to those observed in the high-latitude scintillation observations. Furthermore, *Rino* [1979] did not find any evidence of finite

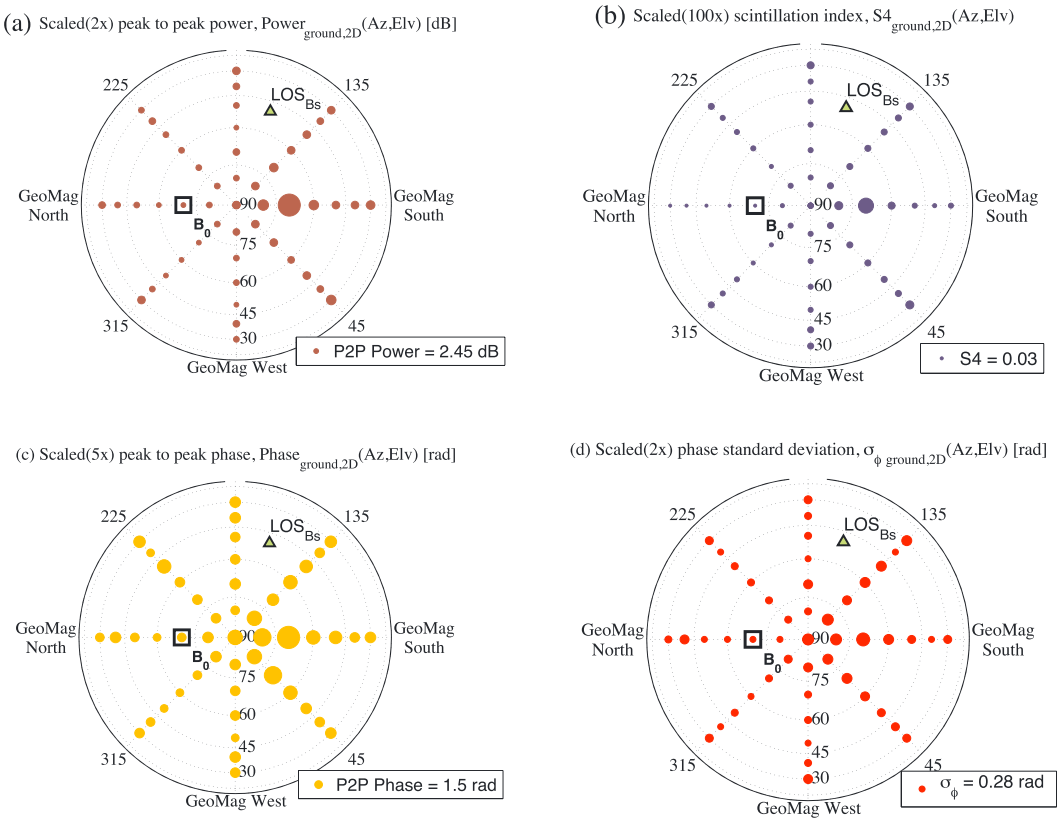

Figure 4. Sensitivity study 1: Sky plots of the SIGMA outputs (S4, P2P power, σ_ϕ, and P2P phase). Elevation angles range from 90° at the center to 0° at the periphery. The concentric circles are constant elevation circles spaced 15° apart. Azimuths vary from 0° to 360° in anticlockwise direction starting at geomagnetic west. The squares indicate the magnetic field (B_0) direction, while the triangle indicates the base value of the LOS vector (LOS_{Bs}).

outer scale cutoffs. This compelled us to believe that the outer scale is a precarious parameter to investigate. We also emphasize here that a full-blown parametric study of all these parameters is out of the scope of this work. Thus, for each sensitivity study, we vary just one parameter at one time keeping the rest of the inputs to their base values. In the following subsections, we present the sensitivity study and detailed analysis with respect to each of the five selected input parameters.

3.1. Effects of the LOS Azimuth and Elevation

The LOS azimuth and elevation angles are the geographical input parameters to SIGMA and can be derived from the satellite and receiver locations. Even in the polar regions, at least seven GPS satellites are available at any instance. Therefore, we believe it is useful to derive the impact of the orientation of a satellite with respect to a receiver in the presence of the magnetic field, on the GNSS signal scintillations.

We illustrate the modeled variations in the P2P power, P2P phase, S4, and σ_ϕ with respect to the elevation and azimuth angles as sky plots shown in Figure 4. The inclination angle θ defined in Figure 1 is complimentary to the elevation angle. The sky plots are generated at the geographic South Pole. According to our local coordinate system in Southern Hemisphere shown in Figure 3b, $+y$ axis is toward the geomagnetic South Pole, $+x$ axis is toward the geomagnetic west, and it corresponds to an azimuth of 0°. The 2-D plane seen in Figure 4 is basically a plane obtained by looking down along z axis in Figure 3b. The magnetic field, B_0, at the geographic South Pole is tilted in $-y$ direction or 270° azimuth with a dip angle of 73°. The dip angle is measured from ground similar to an elevation angle. Thus, in Figure 4, B_0 is shown as a square at an azimuth of 270° and an elevation of 73°.

It can be observed from these figures that the power and phase variations peak when the azimuth and elevation angles of the LOS vector is 90° and 73°, respectively. The reason for a higher variation in this direction was deduced from the 2-D plots on the ground. The 2-D phase plot for this case showed isotropic structures, while for all other cases, the plots displayed anisotropic structures. The 2-D phase plots for two cases

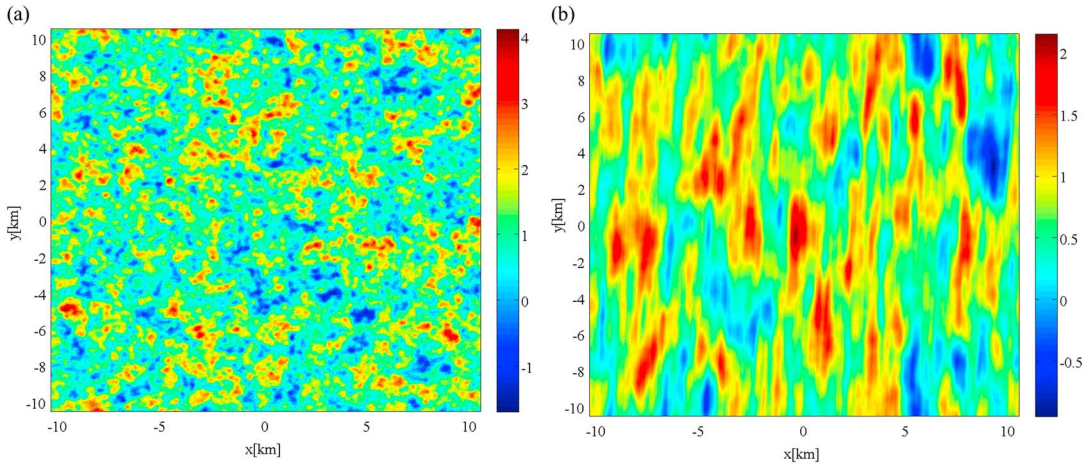

Figure 5. Sensitivity study 1: (a) 2-D phase plots at (azimuth, elevation) = (90°, 73°) showing isotropic structures and (b) 2-D phase plots at (azimuth and elevation) = (160°, 50°) showing anisotropic structures.

(azimuth and elevation) of (90°, 73°) and (160°, 50°) are displayed in Figure 5. We would like to bring to the readers' attention that our base values of the azimuth and elevation angles (160°, 50°) denote a nonpreferred LOS direction (illustrated by a triangle in Figure 4). This can be seen from Figures 4 and 5. Another observation from Figure 4 is that P2P phase shows some high values at 45° and 135° azimuthal directions, but they are not as strong as those in 90° azimuthal direction.

Furthermore, in Figure 6a we investigate the sensitivity of the modeled outputs to the elevation angles for an azimuth of 90°. The P2P power shows a stronger dependence on the elevation angles than the P2P phase. σ_ϕ appears to be more strongly dependent on the elevation angle compared to S4, but as we will quantify later in section 4, it is in fact S4 that displays stronger dependence on the elevation angles than σ_ϕ. We will return to this in detail later in the section 4.

3.2. Effects of Axial Ratio

The axial ratio defines the anisotropy of the field-aligned rod-like irregularities and is basically the length to diameter ratio. *Wernik et al.* [2007] mention that the axial ratio is not a direct observable, and one cannot directly find its values from received data. They also correctly state that not much is known about the anisotropy of the field-aligned irregularities. It is hypothesized that at high latitudes, irregularities are rod shaped, and they decrease in length as the latitude increases. But, it is hard to prove this with a lack of evidence. Additionally, *Wernik et al.* [1990] have found that anisotropy depends on the scale of the irregularities.

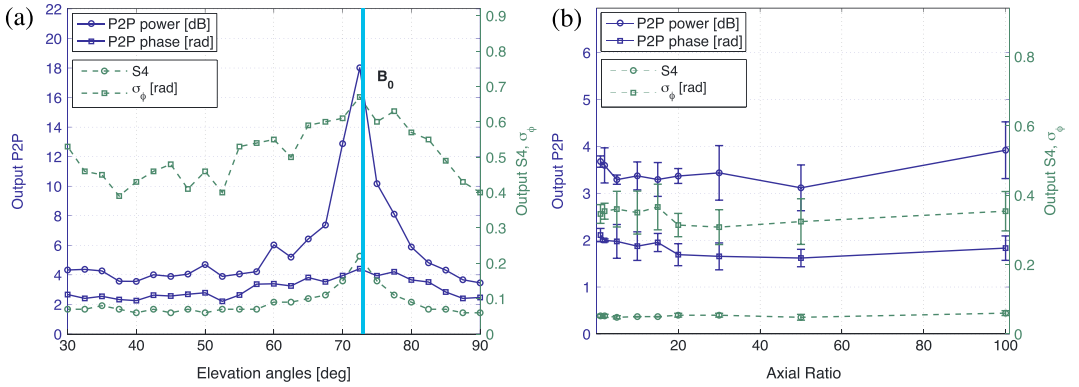

Figure 6. (a) Sensitivity study 1: Dependence of modeled outputs on elevation angles at azimuth of 90°. A line showing the dip angle of 73° at the geographic South Pole is displayed with label B_0. The actual direction of B_0 has an azimuth of 270°. (b) Sensitivity study 2: Dependence of the SIGMA outputs on the axial ratio of the field-aligned irregularity with error bars computed over 50 runs. In both the plots, the solid lines represent the P2P variations, while the dashed lines represent S4 and σ_ϕ.

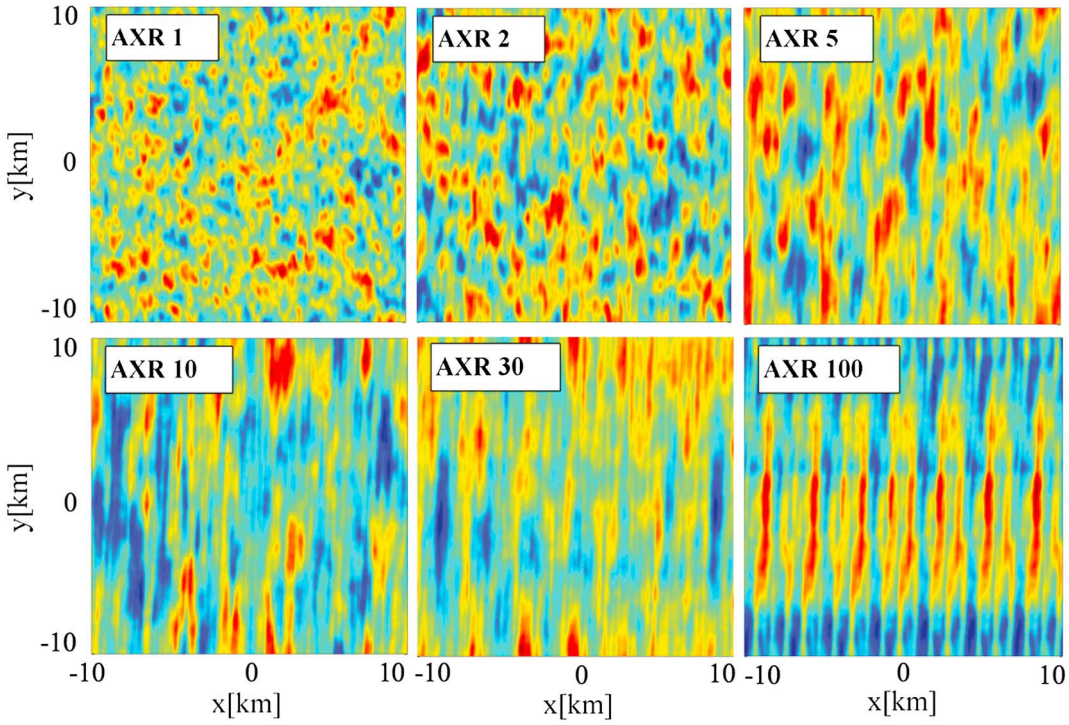

Figure 7. Sensitivity study 3: 2-D phase plots on ground at different axial ratios. Long structures oriented along *y* direction start to appear at high axial ratios.

In spite of this, all the earlier works by Rino as well as SIGMA assume a constant anisotropy for all scale sizes. In this work, we attempt to investigate the axial ratio of the high-latitude irregularities.

Variation of the modeled outputs with respect to the axial ratio is presented in Figure 6b. The error bars in Figure 6b represent the level of variability in our simulation simply due to variations in the random realization of the density structures. They represent the following approximate limits on the accuracy of our simulation results: 1 dB P2P power, 0.5 radians P2P phase, 0.1 radians σ_ϕ, and 0.02 S4. Variations in any of the sensitivity studies that are less than these limits should be considered due to simulation "noise." It should be remembered that the random realizations are based upon statistically independent random variables generated using a completely different seed at each time. The S4 values do not seem to vary much for different runs. The P2P phase and σ_ϕ have a similar trend. Even though it may appear that the outputs remain mostly unchanged as the axial ratio changes, there are higher variations in the outputs at lower axial ratios. For axial ratios greater than or equal to 30, the outputs appear to stabilize. But, a closer examination of the 2-D phase plots for those axial ratios reveals that similar-looking long phase structures oriented almost along the *y* direction start to occur for increasing axial ratios as shown in the set of plots in Figure 7. Additionally, the 2-D plots implied that for the axial ratios lower than 5, the structures look more isotropic.

3.3. Effects of Spectral Index

The spectral index of an irregularity spectrum is an important input parameter. A number of studies have attempted to discern this index from rocket, satellite data, and have proposed several spectral models for high-latitude irregularities [*Dyson et al.*, 1974; *Rufenach*, 1975; *Costa and Kelley*, 1977]. Similar to the axial ratio, the spectral index of an irregularity spectrum cannot be directly measured from the GPS data observed on the ground. We believe that with the help of SIGMA, it will be possible to study the spectral index of an irregularity spectrum for a given scintillation observation. We try to estimate its effect on the observables in this section.

Strangeways [2009] and *Strangeways et al.* [2011] derive the ground spectral indices from the observed S4 and σ_ϕ instead of the high-rate phase and amplitude time histories. We expect to get the high-rate GPS observations to allow us to determine the spectral index on the ground which through the inverse modeling can be related to the irregularity spectral indices.

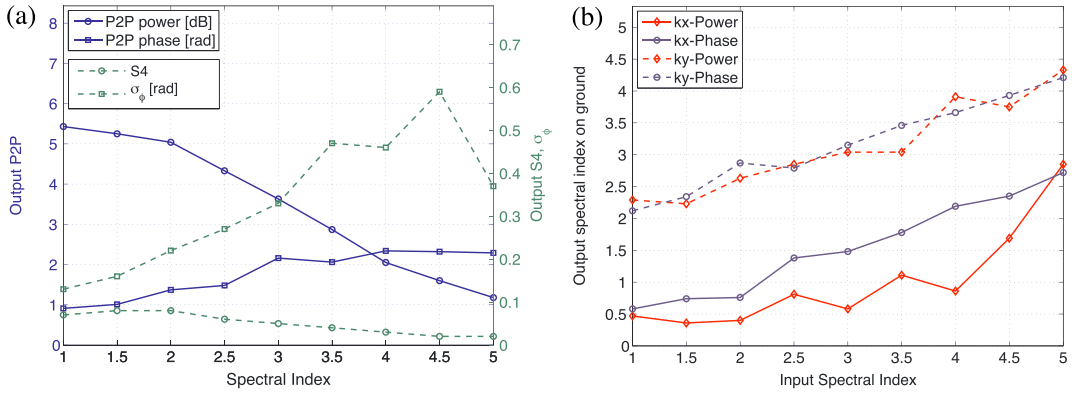

Figure 8. (a) Sensitivity study 3: Sensitivity of the SIGMA outputs with respect to the spectral index. The solid lines represent the P2P variations, while the dashed lines represent S4 and σ_ϕ. (b) Sensitivity study 3: Spectral index on ground plotted against spectral index in the irregularity spectrum. *kx* Power and *ky* Power are the spectral indices on the ground of the spatial spectra of the power in the *x* and *y* directions, respectively. *kx* Phase and *ky* Phase are the spectral indices on the ground of the spatial spectra of the phase in the *x* and *Y* directions, respectively.

As seen from Figure 8a, the P2P phase and σ_ϕ increase slowly with the input (irregularity) spectral index, while the P2P power decreases rapidly with increasing input spectral index. Between spectral index of 3 to 3.5, the P2P phase decreases from 2.2 rad to 2 rad, but σ_ϕ increases from 0.32 rad to 0.48 rad. These variations are within the error bar limits derived from Figure 6b and thus should not be considered as true effects.

In the 2-D phase plots, the 2-D structures appear to be more striated in one direction at lower input spectral index values, while they get more diffused and spread in all directions as the input spectral index increases. In the 2-D power plots, the anisotropy increases as a function of the spectral index. This is the reason for decreasing P2P power with increasing spectral index.

The phase spectrum of the signal received on the ground is generally assumed to have a single slope. The slope of a linear fit to such spectrum can be found between its upper and lower cutoffs on a log-log scale. Examples of the power and phase spatial spectra in the spatial frequency or the wave number domain (*k* space) on the ground in the *x* and *y* directions are displayed in Figure 9. The green straight lines depict the linear fits for each spectra. Spectra in the *x* direction show more jitter compared to that in the *y* direction. Also, a part of the power spectra in the *y* direction between k_f and k_0, closer to k_0, show reduction in the power as the wave number decreases. This could be related to the anisotropy of the irregularity as mentioned by *Strangeways* [2009].

In Figure 8b, we plot the spectral index of the power and phase spectra on the ground in both the *x* and *y* directions as a function of the input spectral index (or the spectral index of the irregularity spectrum).

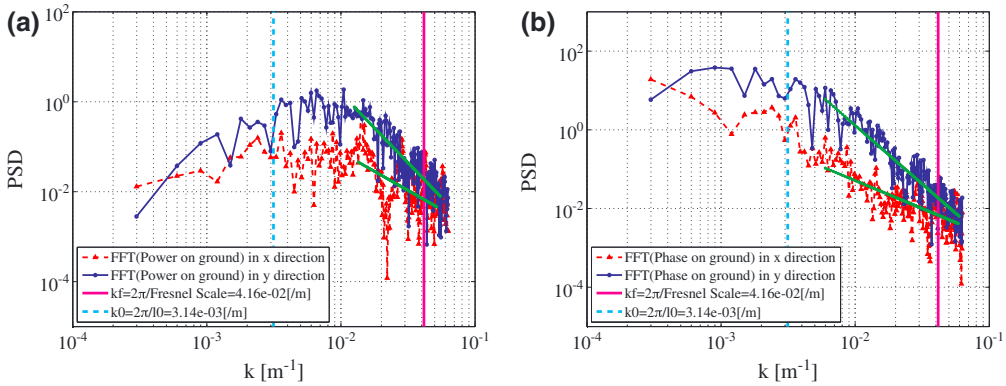

Figure 9. Sensitivity study 3: Examples of (a) power and (b) phase spectra on ground in the *x* and *y* directions. The input spectral index for these plots was equal to 3.

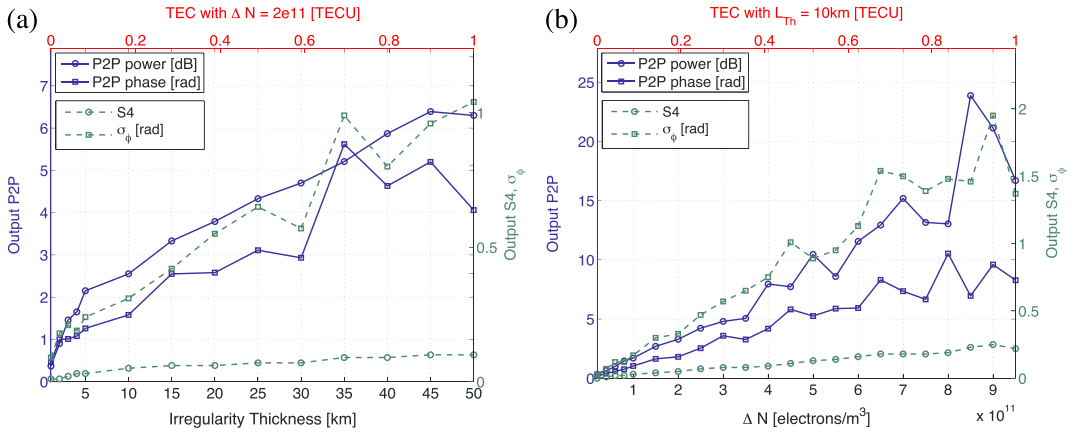

Figure 10. (a) Sensitivity study 4: SIGMA output dependence on the irregularity thickness. The thickness values in TECU are given in upper horizontal axis. (b) Sensitivity study 5: SIGMA output dependence on the RMS electron number density (ΔN) in el/m^3. The ΔN values in TECU are given in upper horizontal axis. In both the plots, the solid lines represent the P2P variations, while the dashed lines represent S4 and σ_ϕ.

The power and phase spectra on the ground display an overall ascending trend. The spectral index on the ground increases with the input spectral index, but the indices in space and on the ground differ from each other.

3.4. Effects of Irregularity Thickness

The phase screen theory assumes that the irregularity is represented as a thin slab [*Yeh and Liu*, 1982]. The change in the phase of the incident wave is proportional to the deviation of the TEC through the slab and thus to the thickness (L_{Th}) of the irregularity as well as the RMS electron density fluctuations (ΔN). Changing the thickness of the layer will reflect in a different irregularity "strength." Thus, a good way to understand the effect of changing the irregularity thickness is to look at the change in the output for a given change in TEC. This can be represented as L_{Th} ΔN in TEC units (TECU), where 1 TECU is equal to 10^{16} el m^{-2}.

In Figure 10a, we present the variations in the SIGMA outputs with respect to L_{Th}. The thickness in kilometers is shown on the lower horizontal axis, while in TECU for the base ΔN is given on the upper horizontal axis. As the thickness of the irregularity increases, the strength of the TEC fluctuations increases, and thus, the phase and power variations increase. This can be seen in Figure 10a.

From 0.1 TECU to 0.8 TECU, which corresponds to the thickness of 10 to 40 km, the P2P power increases with a slope of about 5. Above 0.8 TECU it appears to stabilize, but below 0.1 TECU, the power exhibits a slope of 22. The P2P phase, on the other hand, demonstrates a gradual slope of about 3 between 0.1 TECU and 0.6 TECU. Below 0.1 TECU, it displays a bit higher slope of 7, while above 0.6 TECU, there are sharper variations. An increasing trend similar to P2P power is seen in S4, albeit with very small slopes (< 0.2). Similarly, a trend that looks like that of the P2P phase, although with slope < 1, is seen in σ_ϕ.

The 2-D phase structures look like large patches dispersed in all directions for TECU values smaller than or equal to 0.1 TECU (L_{Th} = 5 km). On the other hand, above 0.1 TECU, the phase structures appear to get thinner in one direction as L_{Th} increases. The 2-D power plots display similar thin structures as the 2-D phase plots.

For this part of the sensitivity analysis, we used a spatial resolution of 200 m in the x and y directions. The reason for this change is to have computationally manageable number of grid points as the size of the simulation box increases with increase in thickness. In the path-integrated phase computation given by equation (4), the number density N_e is computed over the displaced coordinate system governed by the thickness of the layer. Hence, the size of the simulation box increases with thickness.

3.5. Effects of RMS Electron Density Fluctuations

Variation in the RMS electron number density or ΔN changes the strength of the irregularity as explained in section 3.4. Similar to the irregularity thickness, with increasing ΔN, the fluctuations in the phase and power on the ground increase. This can be seen in Figure 10b.

The P2P power graph in Figure 10b can be divided into three parts. The first one up to 0.35 TECU, the second one from 0.35 TECU to 0.7 TECU, and the third one above 0.7 TECU. In terms of ΔN, 0.35 TECU corresponds to 3.5×10^{11} el/m^3 and 0.7 TECU corresponds to 7×10^{11} el/m^3. The first and second parts show somewhat gradual increase with slopes equal to 14 and 29, respectively. Similarly, the P2P phase graph displays slopes equal to 9 and 12 for the first two parts. Although the σ_ϕ plots show similar trend to these two graphs up to 0.7 TECU, a closer examination reveals that the slopes of those first two parts are 2 and 2.5, respectively. S4 appears to have the least dependence on ΔN with very small slopes, close to 0.3. The 2-D plots do not display obvious visual variation in the structure shapes.

For this sensitivity analysis part, we retain the spatial resolution in the *x* and *y* directions as 50 m. Despite of this high spatial resolution, cases where $\Delta N \geq 1 \times 10^{12}$ el/m^3 produce 2-D phase plots with rapidly wrapped phases which are difficult to unwrap properly with our existing algorithms.

4. Discussion

In the previous sections, we describe the electromagnetic propagation through ionospheric electron density perturbation model, SIGMA. We also present the results of a study, based on the use of SIGMA, of the sensitivity of the GNSS scintillation observations on the ground to various physical parameters that describe the irregularity medium. The model itself is different from previous numerical propagation models such as [*Gherm et al.*, 2000, 2005a, 2005b; *Maurits et al.*, 2008; *Béniguel*, 2002; *Béniguel and Hamel*, 2011; *Carrano et al.*, 2011, 2012a] in several important and unique respects. To begin with, the MPS hybrid split-step method is, in principle, an exact numerical implementation of the propagation equations, up to the standard assumptions of the forward scattering and numerical limitations on the minimum spatial resolution. In fact, by stepping through layers and then propagating, we recover the continuous forward scatter integration through the irregularity layer, including arbitrary strong, multiple scattering. This differentiates our model from more approximate wave representations such as *Gherm et al.* [2000, 2005a, 2005b], *Maurits et al.* [2008], and *Béniguel* [2002]. However, the numerical implementation of *Carrano et al.* [2011] and *Carrano et al.* [2012a] is also an MPS hybrid split-step method based on the derivation by *Rino* [2010]. Where we differ from their work is in the exact representation for the arbitrary geometries, including very high latitude geometries. There are several unique features for propagation through the random media at the high-latitude regions. First, since the magnetic field is nearly vertical, and typically, irregularities extend along the field lines to the large scales, the approximation that the layer thickness L_{Th} is much larger than the correlation length ($l_0 \times$ AXR) along the propagation direction is no longer valid. Thus, the calculation of the phase perturbation through an irregularity layer (see equation (4)) has to be done by numerical integration through the layer, and separately for each layer in the MPS approximation.

If the approximation that the layer thickness is much larger than the correlation length along the propagation direction holds true, in SIGMA, we can always go back to the traditional MPS method. In that case, the spatial phase can be obtained by taking the two-dimensional (2-D) inverse Fourier transform of the spectral phase given by the following expression:

$$\Phi(\vec{\kappa}) = \lambda r_e \sec\theta \sqrt{L_{Th}} \sqrt{P_{NH}(k_x, k_y)} \exp(i2\pi\theta_l) \tag{12}$$

where the 3-D power spectrum P_{NH} given by equation (1) is reduced to a 2-D spectrum with a substitution: $k_z = \tan\theta\,(\widehat{\mathbf{a}_\perp} \cdot \vec{\kappa})$. The exponential part imparts a randomness to the fluctuations in the spectral domain. θ_l is a set of statistically independent 2-D random numbers between 0 to 1. In Figure 11, we illustrate the difference between the traditional MPS method and the modified MPS method discussed in section 2. The plots included in this figure are at axial ratios of 5 and 20 for both the traditional and modified MPS methods. For these runs, the SIGMA parameters are as follows: $l_0 = 3$ km, $L_{\mathrm{Th}} = 40$ km, and $\Delta N = 2.5\mathrm{e}11$ (the irregularity strength = 1 TECU). The rest of the parameters with an exception of AXR are the same as the base values given in Table 1. For the axial ratio of 5, the correlation length along the direction of propagation is 15 km. This value is smaller than the thickness of the irregularity, and thus, the plots display similar 2-D phase structures for both the methods. But, when the axial ratio is 20, the correlation length is 60 km. For this case, sharp and unrealistic 2-D phase structures appear along the *y* direction in the 2-D phase plot with traditional MPS method in Figure 11, as against the structures in the phase plot with the modified MPS method. This illustration explains that the traditional MPS method can be used safely when the correlation

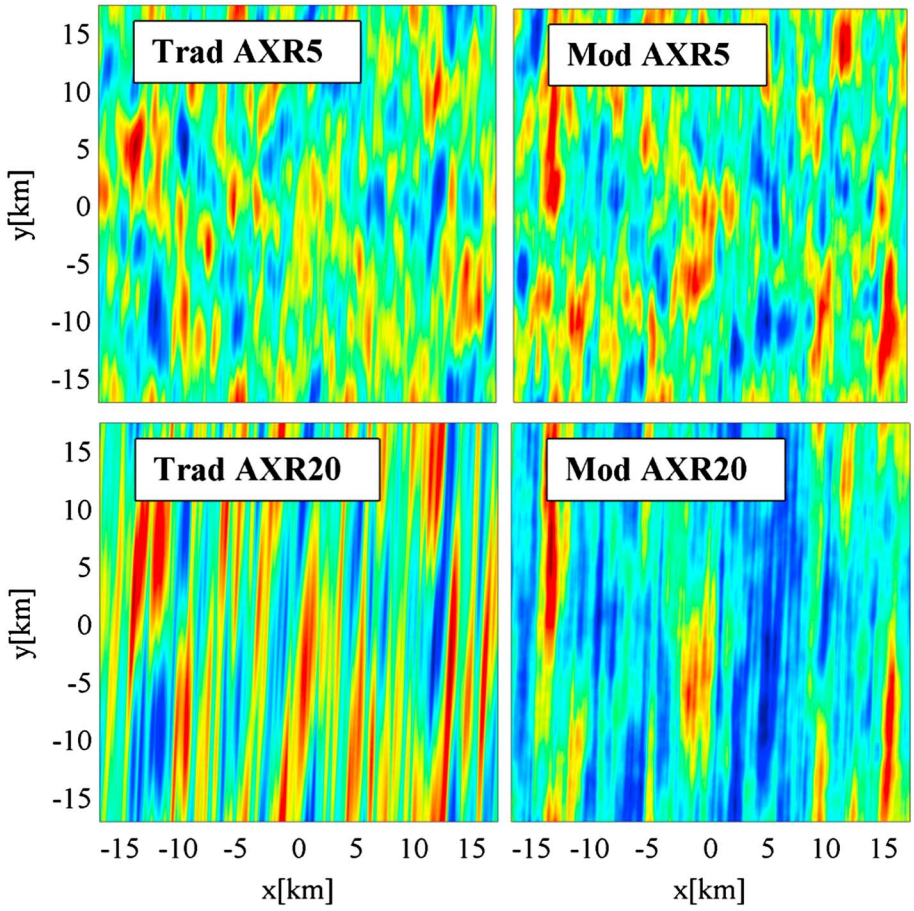

Figure 11. Two-dimensional phase plots on ground for the traditional MPS method and modified MPS method.

length is well below the layer thickness. Additionally, it justifies the application of the modified MPS method in SIGMA for the high-latitude regions whenever the assumption for traditional MPS method is invalid.

The second issue related to the propagation at high latitudes is the arbitrary 3-D geometry. We have our final analysis coordinate system as a local geomagnetic coordinate system, with the "*z* axis" radially outward, *x* to the west, and *y* to the south as shown in Figure 3. But the natural coordinate system for the irregularities is along and perpendicular to the magnetic field. Thus, we have a coordinate transformation that changes anytime we move to a different magnetic dip latitude. This continuously displaced coordinate system has been implemented by *Rino* [2010] and *Carrano et al.* [2012a] before but not for the generalized case of 3-D number density fluctuations discussed in this paper. Finally, we have to account for the slant path of the signal line of sight between the transmitter and receiver on the ground. For very high latitudes the GPS elevation angle is quite low (46° or less at the South Pole). This implies that the horizontal extent of the signal trajectory as it passes through the layer is at least as large as the vertical extent of the layer. For the larger layers, especially in the *F* region, we have to simulate ~100 km or larger horizontal regions, which carries with it its own unique numerical challenges. All of these issues are dealt within SIGMA while still maintaining generality, high accuracy, and fidelity. Thus, SIGMA can be used to study the propagation of the EM waves through the random electron density fluctuations anywhere on the globe and at any altitude. As far as the authors are aware, this global, arbitrary geometry capability is unique to SIGMA. It should be noted that although we are mostly dealing with weak scattering for the Hybrid model selected in this study, SIGMA has capability to work with strong scattering cases as well.

One of the numerical limitation of SIGMA is the minimum resolution we can take in the *x*, *y*, and *z* directions, retaining an expedient amount of the simulation memory and computation time. As mentioned at the beginning of section 3, we are considering the spatial resolutions in decameters. This works well for our purpose, since we are interested in looking at the intermediate-scale structures with scale sizes from

100 m to 100 km. Another numerical limitation of SIGMA is that the computational resources will effectively determine how high an anisotropy ratio we can properly accommodate in a simulation for a given outer scale.

We begin our sensitivity study by examining the statistics of the phase and amplitude variations on the ground with respect to the variations in the signal elevation and azimuth. In section 3.1 we show that there is a peak in the observed parameters when the elevation angle of the LOS vector is equal to the dip angle of the magnetic field and the LOS azimuth was 180° from the azimuth of the magnetic field B_0. To determine whether this is a general effect for any magnetic dip angle, we repeated the test for different receiver locations in the Southern (at 40° dip angle) and Northern Hemispheres (at 50° dip angle). In each case, we noticed a clear peak when the elevation of the LOS vector was equal to the dip angle and the azimuth was in the direction opposite to B_0. We believe that this enhancement in the phase and amplitude scintillations at the dip angle elevation is related to the propagation path geometry and the projection of the plane normal to the LOS vector in the presence of the ionospheric irregularities oriented along an inclined magnetic field. When there is a preferred LOS elevation and azimuth relative to B_0, the 2-D phase and amplitude fluctuations observed on the ground are approximately isotropic, with smaller scales dominant (Figure 5a). By preferred direction we mean, the LOS elevation angle equal to the dip angle and the azimuth angle equal to 180° plus the azimuth of the magnetic field B_0. However, for an arbitrary LOS, the observations are non-isotropic, with one direction having elongated structures relative to the other (Figure 5b). The amount of this elongation will depend on the magnetic dip angle, as well as the aspect ratio of the along-the-field irregularities compared to the irregularities perpendicular to the field. Since there is more random structure for smaller, isotropic scales, there will be higher statistical levels of S4 and P2P for the amplitudes. This analysis is for statistics over a 2-D spatial region. For a more typical case of a time series due to irregularities drifting past the LOS, we would expect higher values of amplitude scintillation when the drift velocity is along the axis with smaller-scale irregularities that is along the magnetic east-west direction. At high latitudes, the structures that cause scintillations (auroral arcs and polar cap patches) are moving in a magnetic north-south direction (toward the pole or away from the pole). This may be one of the reasons for the observed lesser occurrence of strong amplitude scintillations compared to the phase scintillations in those regions [*Aarons*, 1997; *Basu et al.*, 1998; *Mitchell et al.*, 2005; *Kinrade et al.*, 2012; *Deshpande et al.*, 2012; *Kinrade et al.*, 2013], where both the direction and magnitude of the irregularity drift might be the responsible factors.

In sections 3.2, 3.3, 3.4, and 3.5 we investigate the sensitivity of the ground observables to the axial ratio, spectral index, layer thickness, and overall strength of the irregularities, respectively. The goal is to obtain a better understanding of what the observables can tell us about the underlying irregularity structuring. The most interesting result is how the P2P variations in the phase and amplitude depend upon the spectral index of the irregularity spectrum. In Figure 8a, the P2P power is approximately constant for smaller values of spectral index, until the spectral index reaches ~2. For values greater than ~2 to 4, the P2P power falls off quite rapidly. For the P2P phase variation the situation is different. First, the dependence on the spectral index is weaker for the phase. Second, the P2P phase actually increases somewhat with larger spectral index. The case is similar for σ_ϕ and S4, although the dependence of S4 is less pronounced. Another interesting aspect of Figure 8a is the fact that the σ_ϕ seems to peak at the spectral index of ~4.5.

To study the effect of the spectral index in greater detail, we compute the spatial spectra on the ground from the phase and amplitude structuring in both the *x* and *y* directions. The spectral indices of the spectra observed on the ground are expected to be different than those in the irregularity spectra. This is because of the nonlinear transformations on the signal propagating through the irregularity and space. We compute the ground spectra by determining the region where there is an approximately linear decrease in the power with frequency (the inertial subrange). We determine this region by visual inspection of the higher cutoff (close to the Fresnel scale) and lower cutoff (before a roll over). Figure 9 shows an example of the power and phase spectrum and the linear fit. The spectral indices of the phase spectra on the ground in Figure 8b appear to increase with the input spectral index in both the *x* and *y* directions. Both the phase and power spectral indices in the *y* direction increase in a linear fashion, with the ground index *p* given from the irregularity index p_i by the linear relation $p \approx 1.75 + 0.5\, p_i$. This is significantly different from the structure of the observed spectral index on the ground in the *x* direction. First, while the phase spectral index relation is approximately linear, this is not the case for the power index. The power spectral index (red solid curve with diamond markers in Figure 8b) increases slowly for the irregularity spectral indices <4, with the ground

Table 2. SIGMA Sensitivity Study Results in Terms of a Quantitative Parameter: $Q_\beta = (\beta_{max} - \beta_{min})/\beta_{max}$ Where β Is an Observable

Q_β	Elv-Az (Az = 90°)	AXR	*SpInd*	L_{Th}	ΔN
Q_{S4}	0.73	0.17	0.75	0.90	1
Q_{σ_ϕ}	0.42	0.4	0.78	0.91	0.98
$Q_{P2PPower}$	0.81	0.17	0.78	0.94	0.99
$Q_{P2P\phi}$	0.50	0.33	0.61	0.92	0.98

power index ~0.5 to 1. Then, for irregularity spectral indices ranging from 4 to 5, it rapidly increases to almost 3, which is clearly a nonlinear response. The slope of the phase spectral index in the *x* direction is approximately the same as the slopes for the *y* direction, though the zero intercept is closer to 0.

From Figure 3b, we know that the magnetic field is in the $-y$ direction. In other words, the *x* direction is perpendicular to B_0. Thus, we believe that the dissimilarity we see in the *x* and *y* directions in Figure 8b is because of the presence of B_0 and the anisotropy of the irregularity itself. For 3-D isotropic spectra, the relation between the spectral index on the ground in one direction (1D) spectra and the 3-D spectral index is found to be $p = p_i - 1$ [*Yeh and Liu*, 1982], which is different from the relation we are getting. However, for the case under study in this paper we have an anisotropic 3-D spectra, so we do not expect the same result.

Another interesting feature in the sensitivity analysis is the variation in the ground observables with respect to the changes in the axial ratio, for ratios <30. For the larger axial ratios, the coherence length along the *z* axis becomes larger than the thickness of the layer (10 km), and thus, the ratios have no effect on the observations. For the smaller axial ratios there seems to be a definite minimum for an axial ratio of ~20. This exact value of the axial ratio is likely modified by other parameters including the LOS of the signal. Still, Figure 7 demonstrates that the 2-D phase pattern ground observables are sensitive to the axial ratio. Thus, a 2-D array of GPS scintillation receivers capable of imaging the ground phase structure could be used, in combination with SIGMA modeling, to study the axial ratio of irregularities at high latitudes.

The final set of parameters are the layer thickness and the strength of the irregularities. Previous studies [*Booker et al.*, 1985] have shown that the total path-integrated density fluctuations of the layer, given by the product of the irregularity strength and layer thickness, is the relevant parameter for observed scintillations. However, those studies generally assumed the irregularity coherence length along the layer direction (*z* axis) to be much less than the layer thickness. For the high-latitude case where the magnetic field direction is nearly vertical, the coherence length can be several tens of kilometers and comparable to the layer thickness. Thus, the assumption does not necessarily hold. To investigate whether the TEC is the relevant parameter at high latitudes, we separately varied the thickness and irregularity strength. An extra horizontal axis in Figures 10a and 10b is shown in TECU to facilitate the comparison. The slopes with respect to TECU in Figure 10b are higher compared to those in Figure 10a. This is an indicator that the RMS density fluctuation has a stronger effect on the SIGMA outputs than the irregularity thickness. However, an interesting result is that for small layer thicknesses (~5 km or less) the P2P phase and power seem to rise quite rapidly with increasing thickness (Figure 10a); then, for larger thicknesses, the P2P values increase linearly with thickness (as expected), until for very thick layers (>40 km) the P2P power and phase seem to level off or even decrease. A similar but smaller effect is seen in the σ_ϕ in Figure 10a. Interestingly, no such effect is observed for the irregularity strength in terms of ΔN (Figure 10b), which indicates that the two parameters have somewhat different effects upon the observables, and a single product parameter such as TEC is insufficient.

The sensitivity plots obtained from section 3 can be interpreted in different ways. We present Table 2 to quantitatively list out the sensitivity of the individual output parameters to each of the input parameters. The quantity that is presented here is $Q_\beta = (\beta_{max} - \beta_{min})/\beta_{max}$, where β is an observable. It basically exemplifies the spread in each output variable in a sensitivity study, normalized with its maximum value.

Based on the values we obtained in Table 2, our initial question, which of the output parameters gets affected the most in case of varying each of the input parameters individually, can be answered to some extent as follows. From this study, we found that the P2P power gets affected the most for changes in the azimuth and elevation, while changes in axial ratio majorly affect the P2P phase and σ_ϕ. All the observables except the P2P phase are sensitive to the irregularity spectral index, whereas L_{Th} and ΔN influence all the observables.

5. Conclusions and Future Work

In this paper, we have presented a new numerical model for the electromagnetic propagation through the random ionospheric electron density fluctuations. The new model, SIGMA, is a split-step model composed of multiple phase screens and forward propagation between the screens. The new model is entirely general, is applicable anywhere on the globe, and can be used to study scintillations for a wide variety of frequencies ranging from the low VHF (or high HF) through GHz. The salient new features of the model are how it handles the arbitrary 3-D geometries at high latitudes, the extended distribution of irregularities along the field lines, and the low elevation angle signal paths through the irregularities. The model can accept any 3-D realization of the electron density fluctuations from both first principle numerical simulations as well as empirically based spectral models. Consequently, although in the current work, we have used a spectral model of electron density fluctuations that are assumed to be zero-mean stationary random processes, we intend to couple SIGMA with data assimilation techniques and tomography algorithms and use their background densities in SIGMA. Examples of such algorithms and techniques include Ionospheric Data Assimilation Three-Dimensional (IDA3D) algorithm proposed by *Bust et al.* [2004] and Multi-Instrument Data Assimilation System (MIDAS) developed by *Spencer and Mitchell* [2007]. Additionally, it is possible to incorporate time variation of the background density, for example, in the presence of particle precipitation. An important advantage of SIGMA over other statistically based scintillation simulation models is that with density structure realizations, we can achieve propagation simulations with significantly higher fidelity.

The overall long-term research objective is to combine the modeling results from SIGMA with observations of closely clustered arrays of GNSS scintillation receivers at high latitudes. The array of ground observations will allow us to completely determine (or at least highly constrain) the unknown parameters in the spectral model of the irregularity, the altitude, thickness, and drift velocities of the irregularities. However, such a large parameter space can lead to many possible configurations of the spectrum and layer parameters. Thus, the sensitivity study carried out in this paper is designed to help us understand which parameters are the most sensitive (or have the most visibility) to the ground observations. From such a baseline case, we can then iterate on different model realizations until we achieve the best fit between the observations and model predictions. It should be noted that for as few as four scintillation receivers deployed over a baseline of a few kilometers, there are six independent measurements available at each time step (or averaging time). In addition to that, if a measurement of the overall strength of the scintillations is available, this is enough information to determine the irregularity spectral parameters, as well as the height and thickness of the layer, with the use of SIGMA.

Our follow-up paper will focus on comparing SIGMA simulations to high-latitude GNSS observations and achieve a better understanding of the underlying dynamics of the intermediate-scale irregularities producing the observations. In summary, we plan to solve an inverse problem by considering scintillation observations and using SIGMA to determine the best-suited physical and propagation parameters for the irregularity generating these scintillations. We believe this approach will help us understand the polar and auroral irregularity physics.

Acknowledgements

We would like to thank the National Science Foundation for supporting this research under grants ANT-0839858, ATM-922979, PLR-1243398, ANT-0840650, PLR-1248087, and AGS-1311922. K.B. Deshpande is grateful to Sunanda Basu for her valuable suggestions on the irregularity sizes at different altitudes.

Robert Lysak thanks the reviewers for their assistance in evaluating this paper.

References

Aarons, J. (1982), Global morphology of ionospheric scintillations, *Proc. IEEE*, *70*(4), 360–378.

Aarons, J. (1997), Global positioning system phase fluctuations at auroral latitudes, *J. Geophys. Res.*, *102*, 17,219–17,232, doi:10.1029/97JA01118.

Basu, S., E. J. Weber, T. W. Bullett, M. J. Keskinen, E. MacKenzie, P. Doherty, R. Sheehan, H. Kuenzler, P. Ning, and J. Bongiolatti (1998), Characteristics of plasma structuring in the cusp/cleft region at Svalbard, *Radio Sci.*, *33*, 1885–1900, doi:10.1029/98RS01597.

Béniguel, Y. (2002), Global Ionospheric Propagation Model (GIM): A propagation model for scintillations of transmitted signals, *Radio Sci.*, *37*, RS1032, doi:10.1029/2000RS002393.

Béniguel, Y., and P. Hamel (2011), A global ionosphere scintillation propagation model for equatorial regions, *J. Space Weather Space Clim.*, *1*(26), A04, doi:10.1051/swsc/2011004.

Booker, H. G., J. A. Ferguson, and H. O. Vats (1985), Comparison between the extended-medium and the phase-screen scintillation theories, *J. Atmos. Terr. Phys.*, *47*, 381–399.

Bust, G. S., T. W. Garner, and T. L. Gaussiran (2004), Ionospheric Data Assimilation Three-Dimensional (IDA3D): A global, multisensor, electron density specification algorithm, *J. Geophys. Res.*, *109*, A11312, doi:10.1029/2003JA010234.

Carrano, C. S., K. M. Groves, R. G. Caton, C. L. Rino, and P. R. Straus (2011), Multiple phase screen modeling of ionospheric scintillation along radio occultation raypaths, *Radio Sci.*, *46*, RS0D07, doi:10.1029/2010RS004591.

Carrano, C. S., K. M. Groves, and R. G. Caton (2012a), Simulating the impacts of ionospheric scintillation on L band SAR image formation, *Radio Sci.*, *47*, RS0L20, doi:10.1029/2011RS004956.

Carrano, C. S., C. E. Valladares, and K. M. Groves (2012b), Latitudinal and local time variation of ionospheric turbulence parameters during the conjugate point equatorial experiment in Brazil, *Int. J. Geophys.*, *2012*, 103963, doi:10.1155/2012/103963.

Costa, E., and S. Basu (2002), A radio wave scattering algorithm and irregularity model for scintillation predictions, *Radio Sci.*, *37*(3), 1046, doi:10.1029/2001RS002498.
Costa, E., and M. C. Kelley (1977), Ionospheric scintillation calculations based on in situ irregularity spectra, *Radio Sci.*, *12*, 797–809, doi:10.1029/RS012i005p00797.
Deshpande, K. B., G. S. Bust, C. R. Clauer, H. Kim, J. E. Macon, T. E. Humphreys, J. A. Bhatti, S. B. Musko, G. Crowley, and A. T. Weatherwax (2012), Initial GPS Scintillation results from CASES receiver at South Pole, Antarctica, *Radio Sci.*, *47*, RS5009, doi:10.1029/2012RS005061.
Dyson, P. L., J. P. McClure, and W. B. Hanson (1974), In situ measurements of the spectral characteristics of F region ionospheric irregularities, *J. Geophys. Res.*, *79*, 1497–1502, doi:10.1029/JA079i010p01497.
Fremouw, E. J., and J. A. Secan (1984), Modeling and scientific application of scintillation results, *Radio Sci.*, *19*, 687–694, doi:10.1029/RS019i003p00687.
Ghafoori, F. (2012), Modeling the impact of equatorial ionospheric irregularities on GPS receiver performance, PhD thesis, Dept. of Geomatics Engineering, Univ. of Calgary, Calgary, Alberta, Canada.
Gherm, V. E., N. N. Zernov, S. M. Radicella, and H. J. Strangeways (2000), Propagation model for signal fluctuations on transionospheric radio links, *Radio Sci.*, *35*, 1221–1232, doi:10.1029/1999RS002301.
Gherm, V. E., N. N. Zernov, and H. J. Strangeways (2005a), Propagation model for transionospheric fluctuating paths of propagation: Simulator of the transionospheric channel, *Radio Sci.*, *40*, RS1003, doi:10.1029/2004RS003097.
Gherm, V. E., N. N. Zernov, and H. J. Strangeways (2005b), HF propagation in a wideband ionospheric fluctuating reflection channel: Physically based software simulator of the channel, *Radio Sci.*, *40*, RS1001, doi:10.1029/2004RS003093.
Gola, M., A. W. Wernik, S. J. Franke, C. H. Liu, and K. C. Yeh (1992), Behaviour of HILAT scintillation over Spitsbergen, *J. Atmos. Terr. Phys.*, *54*, 1207–1213.
Gondarenko, N. A., and P. N. Guzdar (2001), Three-dimensional structuring characteristics of high-latitude plasma patches, *J. Geophys. Res.*, *106*, 24,611–24,620, doi:10.1029/2000JA000440.
Gondarenko, N. A., and P. N. Guzdar (2003), Structure of turbulent irregularities in high-latitude plasma patches—3D nonlinear simulations, in *Disturbances in Geospace: The Storm-substorm Relationship, Geophys. Monogr. Ser.*, vol. 142, edited by A. S. Sharma, Y. Kamide, and G. S. Lakhina, pp. 205–216, AGU, Washington, D. C., doi:10.1029/142GM17.
Gondarenko, N. A., and P. N. Guzdar (2006), Nonlinear three-dimensional simulations of mesoscale structuring by multiple drives in high-latitude plasma patches, *J. Geophys. Res.*, *111*, A08302, doi:10.1029/2006JA011701.
Grimault, C. (1998), A multiple phase screen technique for electromagnetic wave propagation through random ionospheric irregularities, *Radio Sci.*, *33*, 595–606, doi:10.1029/97RS03552.
Humphreys, T. E., M. L. Psiaki, and P. M. Kintner (2010), Modeling the effects of ionospheric scintillation on GPS carrier phase tracking, *IEEE Trans. Aerosp. Electron. Syst.*, *46*, 1624–1637, doi:10.1109/TAES.2010.5595583.
Keskinen, M. J. (2006), GPS scintillation channel model for the disturbed low-latitude ionosphere, *Radio Sci.*, *41*, RS4003, doi:10.1029/2005RS003442.
Keskinen, M. J., S. L. Ossakow, and B. G. Fejer (2003), Three-dimensional nonlinear evolution of equatorial ionospheric spread-F bubbles, *Geophys. Res. Lett.*, *30*, 1855, doi:10.1029/2003GL017418.
Keskinen, M. J., S. L. Ossakow, B. G. Fejer, and J. Emmert (2006), Evolution of equatorial ionospheric bubbles during a large auroral electrojet index increase in the recovery phase of a magnetic storm, *J. Geophys. Res.*, *111*, A02303, doi:10.1029/2005JA011352.
Kinrade, J., C. N. Mitchell, P. Yin, N. Smith, M. J. Jarvis, D. J. Maxfield, M. C. Rose, G. S. Bust, and A. T. Weatherwax (2012), Ionospheric scintillation over Antarctica during the storm of 5-6 April 2010, *J. Geophys. Res.*, *117*, A05304, doi:10.1029/2011JA017073.
Kinrade, J., C. N. Mitchell, N. D. Smith, Y. Ebihara, A. T. Weatherwax, and G. S. Bust (2013), GPS phase scintillation associated with optical auroral emissions: First statistical results from the geographic South Pole, *J. Geophys. Res. Space Physics*, *118*, 2490–2502, doi:10.1002/jgra.50214.
Knepp, D. L. (1983), Multiple phase-screen calculation of the temporal behavior of stochastic waves, *Proc. IEEE*, *71*(6), 722–737.
Knepp, D. L., and L. J. Nickisch (2009), Multiple phase screen calculation of wide bandwidth propagation, *Radio Sci.*, *44*, RS0A09, doi:10.1029/2008RS004054.
Maurits, S. A., V. E. Gherm, N. N. Zernov, and H. J. Strangeways (2008), Modeling of scintillation effects on high-latitude transionospheric paths using ionospheric model (UAF EPPIM) for background electron density specifications, *Radio Sci.*, *43*, RS4001, doi:10.1029/2006RS003539.
Mitchell, C. N., L. Alfonsi, G. De Franceschi, M. Lester, V. Romano, and A. W. Wernik (2005), GPS TEC and scintillation measurements from the polar ionosphere during the October 2003 storm, *Geophys. Res. Lett.*, *32*, L12S03, doi:10.1029/2004GL021644.
Rino, C. (2010), *The Theory of Scintillation With Applications in Remote Sensing*, John Wiley, New York.
Rino, C. L. (1979), A power law phase screen model for ionospheric scintillation I—Weak scatter, *Radio Sci.*, *14*, 1135–1145, doi:10.1029/RS014i006p01135.
Rino, C. L., and C. S. Carrano (2011), The application of numerical simulations in Beacon scintillation analysis and modeling, *Radio Sci.*, *46*, RS0D02, doi:10.1029/2010RS004563.
Rufenach, C. L. (1975), Ionospheric scintillation by a random phase screen: Spectral approach, *Radio Sci.*, *10*, 155–165, doi:10.1029/RS010i002p00155.
Secan, J. A., R. M. Bussey, E. J. Fremouw, and S. Basu (1995), An improved model of equatorial scintillation, *Radio Sci.*, *30*, 607–618, doi:10.1029/94RS03172.
Secan, J. A., R. M. Bussey, E. J. Fremouw, and S. Basu (1997), High-latitude upgrade to the Wideband ionospheric scintillation model, *Radio Sci.*, *32*, 1567–1574, doi:10.1029/97RS00453.
Shkarofsky, I. P. (1968), Generalized turbulence space-correlation and wave-number spectrum-function pairs, *Can. J. Phys.*, *46*, 2133–2153, doi:10.1139/p68-562.
Spencer, P. S. J., and C. N. Mitchell (2007), Imaging of fast moving electron-density structures in the polar cap, *Ann. Geophys.*, *50*, 427–434.
Strangeways, H. J. (2009), Determining scintillation effects on GPS receivers, *Radio Sci.*, *44*, RS0A36, doi:10.1029/2008RS004076.
Strangeways, H. J., Y.-H. Ho, M. H. O. Aquino, Z. G. Elmas, H. A. Marques, J. F. G. Monico, and H. A. Silva (2011), On determining spectral parameters, tracking jitter, and GPS positioning improvement by scintillation mitigation, *Radio Sci.*, *46*, RS0D15, doi:10.1029/2010RS004575.
Wernik, A. W., M. Gola, C. H. Liu, and S. J. Franke (1990), High-latitude irregularity spectra deduced from scintillation measurements, *Radio Sci.*, *25*, 883–895, doi:10.1029/RS025i005p00883.
Wernik, A. W., L. Alfonsi, and M. Materassi (2007), Scintillation modeling using in situ data, *Radio Sci.*, *42*, RS1002, doi:10.1029/2006RS003512.
Yeh, K. C., and C.-H. Liu (1982), Radio wave scintillations in the ionosphere, *Proc. IEEE*, *70*(4), 324–360.